International Journal of Applied Engineering Research ISSN 0973-4562 Volume 10, Number 23 (2015) pp 43794-43800

Computational Aero-acoustic Analysis of a Simplified Vehicle Model at Various Rear Slant angles

Rajkumar Vishnu Ganesh, Yagnavalkya Mukkamala*, Karan Raul Viegas, S. Venkatraghavan

School of Mechanical and Building Sciences, VIT University, Vellore 632014, India
**Corresponding Author Email: yagnasmukkamala@vit.ac.in*

Abstract
The influence of rear slant angle on flow structure is investigated by performing a computational fluid dynamic (CFD) analysis on a simplified vehicle model (Ahmed body). The rear slant angle was varied as 25°, 30° and 35°, with the body subjected to inlet velocities of 140 km/h and 180 km/h at 0° yaw angle. Through this study, we hope to understand the relationship between sound pressure levels at the three pillars of the body with the drag coefficient and rear slant angle. The results provide insight into how the vehicle exterior geometry can be optimized to alleviate aerodynamic noise, which is a major hindrance to ride comfort, while maintaining minimal drag.

Keywords — ahmed body; aero-acoustics; k-e RNG; LES; FW-H

I. INTRODUCTION

Aerodynamic noise is becoming an increasingly pressing problem and is today recognized as a factor influencing the commercial success of passenger vehicles. This problem is known to be especially noticeable in hybrid or electric cars, where engine noise is absent. At high speeds, wind noise becomes more significant, making it difficult to hear or converse inside the cabin, even causing fatigue over long periods. At speeds over 80 km/h, the increase in aerodynamic noise is proportional to the order of V^6, as compared to the increase in other noises which is proportional to the order of V^1-V^3, where V is the speed of the vehicle. This noise originates from sources at numerous parts of the vehicle, at intensities that have been found to vary with factors like external shape and vehicle.

85% of the total drag acting on the body is due to pressure drag, the rest being friction drag. [1] The pressure drag depends on rear slant angle α, and is responsible for 91% of the total pressure drag. At two critical angles 12.5° and 30°, flow structure changes significantly. For angles less than 12.5°, the flow over the rear slanted portion remains fully attached till the trailing edge. At 12.5°, the drag is least. Between 12.5° and 30°, flow over the rear slanted surface becomes highly three-dimensional. Pressure drag increases with rear slant angle α and becomes maximum for α=30°.

Ahmed et al. [1] analyzed time-averaged wake structure around the Ahmed body at Reynolds number of 1.2×10^6 by varying rear slant angle α between 0° and 40°. Their studies are based on the time-averaged flow data and do not give information about unsteady flow characteristics around the Ahmed body. Bayraktar et al. [2] studied the external aerodynamics of the Ahmed body for slant angles of 0°, 12.5°, and 25°. Their concern was the effect of Reynolds number on drag and lift coefficients and the calculation of wind-averaged drag coefficients. Lienhart et al. [3] obtained experimental measurements done in the LSTM low speed wind tunnel using a 2-component laser-Doppler anemometer (LDA) for α=25° and 35° at an air velocity of 40 m/s. But they do not include unsteady analysis of the flow field and investigation of the flow for the critical slant angle of α=30°. Conan et al. [4] studied the influence of rear slant angle on the drag coefficient C_d of the Ahmed body by changing the rear slant angle α from 10° to 40° using PIV and oil visualization techniques.

As stated earlier, for noise generation from dipole acoustic sources, aerodynamic sound intensity increases with vehicle speed. At speeds above 60 km/h, Reynolds number independency is exhibited. [5] The generation of noise at the A, B and C-pillars is due to breakdown of vortex flow geometry, with the source within the shear layer wall region. Alam's studies agree with studies by Mohsen et al. [6] which suggest that pressure fluctuation is highest in the irrotational reattachment region of the flow, and with studies by and Watanabe et al. [7] which attribute aerodynamic sound pressure fluctuation to the vortex core rotational separation region of the flow. The flow separation due to body shape is the main cause of wind noise, and the reduction of airflow velocity at the pillar regions result in the suppression of wind noise. Murad et al. [8] observed from computational results, the generation of trailing edge and boundary layer noise at the A-pillar region, caused by turbulent airflow separation on the side window. While trailing edge noise is dominant during the initial stage of noise propagation, boundary layer noise dominates at the later stage as the flow becomes steadier.

Of all the factors that wind noise primarily depends on viz. shape, speed, wind direction towards the car and the natural wind condition, the car shape is the most influential and controllable factor. Since the external shape of a commercial car is decided during the design stages itself, it is essential to investigate the problem areas by computational methods in order to make adaptations to the design as early as possible, a benefit which is not offered by wind tunnel tests. Lokhande et al. [9] have suggested that k-ε turbulence model be used for aerodynamic characteristics and LES turbulence model be used for the analysis of aero-acoustic characteristics.

In this study, we analyze noise propagation created due to fluctuating air flow at the A, B and C pillar regions of a Simplified Vehicle Model, with rear slant angle α=25, 30 and 35 and for two velocities i.e. 140 km/h and 180 km/h.

II. METHODOLOGY

A. *Geometry Description*

The geometry model is the bluff body as modeled by Ahmed [1] is shown in Fig. 1. The total length of the body is 1044mm and the height is 338mm. A clearance of 50mm is present with the wheels modeled as vertical cylinders of 30mm diameter. The angle of inclination φ at the rear portion, also known as the rear slant angle, has been varied. The rear slant angle is varied as 25°, 30° and 35°.

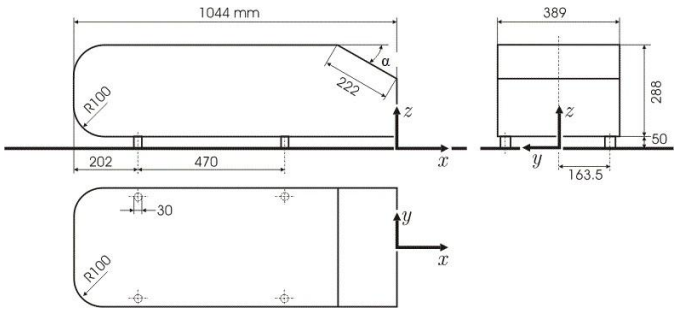

Fig. 1 Ahmed Body

B. *Mesh Description*

The meshing was performed on ICEM CFD. Edge sizing, face sizing, meshing were employed to refine the mesh at various regions as shown in Fig. 2. In order to capture the flow at regions where boundary layer separation is likely to occur, a prism layer refinement area was introduced. A programme-controlled inflation with first aspect ratio of 5 (the first prism layer has a height of 1/5th the surface mesh length) was used. For the purposes of this study, the number of layers was set to five with a geometric growth rate of 1.2. A 9.2m x 3.05m x 3m enclosure was modelled around the geometry to represent the air domain, such that one of its walls divided the body into two halves. This is done as the problem concerned is symmetric in nature and thus computation can be optimised. Ultimately, the number of elements in the mesh was approximately 3.2 million.

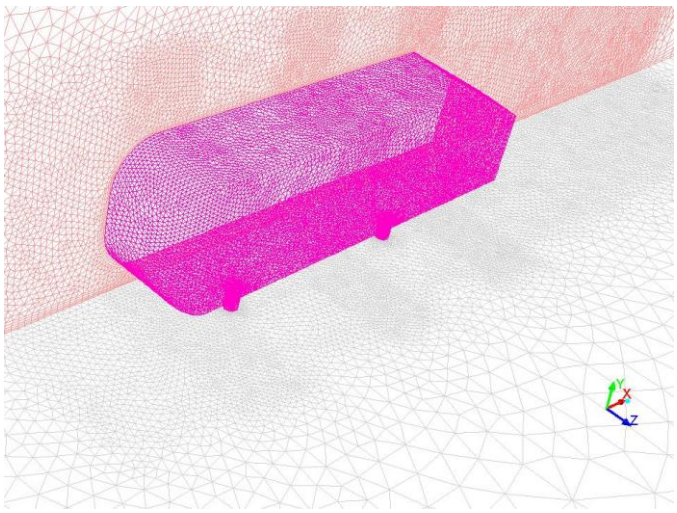

Fig. 2. Three-dimensional mesh of the Ahmed body

C. *Computational Methodology*

1) *RNG k-ε Model:*

The renormalization group theory is used on the instantaneous Navier Stokes equation to derive RNG model [10]. The extra ε term improves the accuracy for rapidly strained flows. The RNG model accommodates the effect of swirl on turbulence thereby enhancing accuracy for swirling flows. While the standard k-ε model uses user specified values, the RNG theory provides an analytical formula for turbulent Prandtl numbers. The RNG theory provides for an analytically derived differential formula that counts for low Reynolds number for effective viscosity unlike the standard k-ε model which is based on high Reynolds number. Effective usage however depends on appropriate treatment of the near wall region. Transport equations for the RNG k-ε model have a similar form to the standard k-ε model.

$$\frac{\partial(pk)}{\partial t}+\frac{\partial}{\partial x_i}(\rho k u_i)=\frac{\partial}{\partial x_j}\left(a_k\mu_{eff}\frac{\partial k}{\partial x_j}\right)+G_k+G_b-\rho\varepsilon-Y_M+S_K \quad (1)$$

$$\frac{\partial}{\partial t}(\rho\varepsilon)+\frac{\partial}{\partial x_i}(\rho\varepsilon u_i)=\frac{\partial}{\partial x_j}\left(a_\varepsilon\mu_{eff}\frac{\partial\varepsilon}{\partial x_j}\right)+C_{1\varepsilon}\frac{\varepsilon}{k}(G_k+C_{3\varepsilon}G_b)-C_{2\varepsilon}\rho\frac{\varepsilon^2}{k}-R_\varepsilon+S_\varepsilon \quad (2)$$

In the above equations, G_b is the generation of turbulent kinetic energy due to buoyancy,G_k represents the generation of turbulent kinetic energy due to the mean velocity gradients, Y_M represented the contribution of the fluctuating dilatation in compressible turbulence to the overall dissipation rate. a_k and a_ε represent the inverse Prandtl numbers for k and ε. S_k and S_ε are user defined source terms.

Modeling the effective viscosity [10]: On applying the scale elimination procedure in RNG theory, a differential equation for turbulent viscosity is obtained, as

$$d\left(\frac{\rho^2 k}{\sqrt{\varepsilon\mu}}\right)=1.72\frac{\hat{v}}{\sqrt{\hat{v}^3-1+C_v}}d\hat{v} \quad (3)$$

Where,

$$\hat{v}=\frac{\mu_{eff}}{\mu}$$

Eq. (3) is integrated to obtain an accurate description of how effective turbulent transport varies with the effective Reynolds number (or eddy scale), therefore making the model better equipped to handle low-Reynolds number and near wall flows.

Eq. (3) in the high-Reynolds number limit gives,

$$\mu_t=\rho C_\mu\frac{k^2}{\varepsilon}$$

Where C_μ=0.0845, which is derived using RNG theory. Moreover the value of C_μ is very close to the empirically determined value of 0.09, used in standard k-ε model.

Model constants: The model constants $C_{1\varepsilon}$ and $C_{2\varepsilon}$ have values analytically derived by the RNG theory.

$$C_{1\varepsilon}=42,\ C_{2\varepsilon}=1.68$$

2) Large Eddy Simulation (LES):

Turbulent flows are composed of large eddies comparable in size to the characteristic length of mean flow and smaller ones that lead to the dissipation of turbulent kinetic energies.

In LES as opposed to DNS which leads to high computing time and cost (proportional to Re_t^3 where Re_t is the turbulent Reynolds number), large eddies are resolved directly and smaller ones are modeled. In terms of the fraction of resolved scales LES falls between DNS and RNS. LES is preferred since the momentum, mass, energy and other passive scalars are transported by large eddies which are dictated by geometry and boundary conditions. Small eddies however tend to be isotropic and less dependent on geometry. Therefore coarse mesh can be used to resolve larger eddies and larger time-step sizes are used in LES as opposed to DNS.

a) Subgrid-Scale Models:

The Boussinesq hypothesis is employed for subgrid-scale turbulence models by ANSYS Fluent in the RANS models for computing subgrid-scale turbulent stresses from

$$\tau_{ij}-\frac{1}{3}\tau_{kk}\delta_{ij}=-2\mu_t\overline{S}_{ij} \tag{4}$$

Where μ_t is the subgrid-scale turbulent viscosity. The isotropic part of the subgrid-scale stresses τ_{kk} is not modeled, but added to the filtered static pressure term. The rate-of-strain tensor for the resolved scale $\overline{S}_{ij}$ is defined by

$$\overline{S}_{ij}\ \equiv\ \frac{1}{2}\left(\frac{\partial\overline{u}_i}{\partial x_j}+\frac{\partial\overline{u}_j}{\partial x_i}\right) \tag{5}$$

For compressible flows density-weighted (or Favre) filtering operator is used :

$$\widetilde{\emptyset}=\frac{\overline{\rho\emptyset}}{\overline{\rho}} \tag{6}$$

The compressible form of the subgrid stress tensor is defined as:

$$\tau_{ij}=\overline{\rho}\widetilde{u_iu_j}-\overline{\rho}\tilde{u}_i\tilde{u}_j \tag{7}$$

This term is split into its isotropic and deviatoric parts

$$\tau_{ij}=\tau_{ij}-\frac{1}{3}\tau_{kk}\delta_{ij}+\frac{1}{3}\tau_{kk}\delta_{ij} \tag{8}$$

The deviatoric part of the subgrid-scale stress tensor is modeled using the compressible form of the Smagorinsky model:

$$\tau_{ij}-\frac{1}{3}\tau_{kk}\delta_{ij}=-2\mu_t(S_{ij}-\frac{1}{3}S_{kk}\delta_{ij}) \tag{9}$$

The term involving τ_{kk} can be added to the filtered pressure or simply neglected for incompressible flows. This term can be rewritten as $\tau_{kk}=\gamma M_{sgs}^2\overline{p}$ where M_{sgs} is the subgrid Mach number which is expected to be small when the turbulent Mach number of the flow is small.

The modeling of the subgrid-scale turbulent flux of a scalar ∅, is done using a subgrid-scale turbulent Prandtl number

$$q_j=-\frac{\mu_t}{\sigma_t}\frac{\partial\emptyset}{\partial x_j} \tag{10}$$

Where q_j is the subgrid-scale flux.

The modelling of the compressible subgrid enthalpy flux term is done in the same manner

$$\overline{\rho}\left(\widetilde{u_ih_s}-\tilde{u}_i\tilde{h}_s\right)=-\frac{\mu_{SGS}C_p}{Pr_{SGS}}\frac{\partial\tilde{T}}{\partial x_j} \tag{11}$$

Where μ_{SGS} is a subgrid viscosity, h_s is the sensible enthalpy and Pr_{SGS} is a subgrid Prandtl number equal to 0.85.

b) Smagorinsky-Lilly Model

Proposed by Smagorinsky, the eddy viscosity is modelled by

$$\mu_t=\rho L_S^2\left|\overline{S}\right| \tag{12}$$

Where $\left|\overline{S}\right|\equiv\sqrt{2\overline{S}_{ij}\overline{S}_{ij}}$ and L_S is the mixing length for subgrid scales. L_S is computed using

$$L_S=\min(\kappa d,C_S\Delta)$$

Where d is the distance to the closest wall, C_S is the Smagorinsky constant, κ is the Von Karman constant and is the local grid scale. In ANSYS $\Delta=V^{1/3}$

A value of 0.23 was derived by Lilly for C_S for homogenous isotropic turbulence in the inertial subrange.However this value, in the presence of mean shear and in transitional flows as near solid boundary, caused excessive damping of large scale fluctuations and thus has to be reduced in such regions. Hence C_S is not auniversal constant, nonetheless a C_S value of around 0.1 has been found to yield the best results for a wide range of flows.

3) Ffowcs-Williams and Hawkings (FW-H) formulation

ANSYS Fluent offers a method based on the Ffowcs-Williams and Hawkings (FW-H) model [11] which uses Lighthill's acoustic analogy, given by Layton et al. [12]., to predict sound generated by equivalent acoustic sources. ANSYS Fluent adopts a time domain integral formulation wherein time histories of acoustic signals, at prescribed receiver locations are computed using surface integrals.

It is an inhomogeneous wave equation derived by manipulating the continuity equation and Navier-Stokes Equations.

$$\frac{1}{a_0^2}\frac{\partial^2 p'}{\partial t^2} - \nabla^2 p' = \frac{\partial^2}{\partial x_i \partial x_j}\{T_{ij}\, H(f)\}$$

$$- \frac{\partial}{\partial x_i}\{[P_{ij} n_j + \rho u_i (u_n - v_n)]\delta(f)\}$$

$$+ \frac{\partial}{\partial t}\{[\rho_0 v_n + \rho(u_n - v_n)]\delta(f)\} \quad (13)$$

Where
u_i=fluid velocity component in the x_i direction
u_n=fluid velocity component normal to the surface f=0
v_i=surface velocity components in the x_i direction
v_n=surface velocity component normal to the surface
$\delta(f)$=Dirac delta function
$H(f)$=Heaviside function

The sound pressure at the far field is denoted by p' ($p'=p-p_o$). A mathematical surface denoted by $f=0$ is introduced to "embed" the exterior flow problem ($f>0$) in an unbound space. This facilitates the use of a generalized function theory and the free-space Green function to obtain the solution. The surface ($f=0$) assumes the role of source (emission) surface, and can be made coincident with a body (impermeable) surface or a permeable surface off the body surface. a_o is the far-field sound speed, n_i is the unit normal vector pointing toward the exterior region ($f>0$), and T_{ij} is the Lighthill stress tensor, defined as

$$T_{ij}=\rho u_i u_j + P_{ij} - a_0^2(\rho-\rho_0)\,\delta_{ij} \quad (14)$$

P_{ij}=the compressive stress tensor.
For a Stokesian fluid, this is given by

$$P_{ij}=p\delta_{ij} - \mu\left[\frac{\partial u_i}{\partial x_j} + \frac{\partial u_j}{\partial x_j} - \frac{2}{3}\frac{\partial u_k}{\partial x_k}\delta_{ij}\right] \quad (15)$$

The Transient fluctuations of the surface pressure of the Ahmed body, which is considered to be the primary noise source in this study, is computed by a unsteady analysis utilizing the Large Eddy Simulation, which would provide the inputs for obtaining a solution using FW-H equation. [11] The dominating sources in this study can be categorized as dipole sources, arising out of fluid structure interaction. The pressure signals thus obtained at the A-, B-, C-Pillar regions are post processed using a Fast Fourier Transform routine to compute the Sound pressure levels at different receiver locations. The time history of the signals is translated to Frequencies. Being logarithmic measures of sound relative sound pressure, the sound pressure levels are converted to dB units using,

$$L_p = 20 log_{10}\left(\frac{p}{p_o}\right) dB \quad (16)$$

III. RESULTS AND DISCUSSION

A. *Validation Study*

In order to validate the accuracy and legitimacy of the software and methodology employed, the numerical results for the case of an Ahmed body with a rear slant angle α=25° have been corroborated with experimental results for the same. The experimental results have already been produced by Ahmed et al. which include the time averaged wake structure around the Ahmed body at Reynolds number Re=1.2 x 10^6 and rear slant angle of 25°. The k-εturbulence model was performed for the above stated conditions and the results obtained closely resemble those of Ahmed, with a variation of 6.9% for the value of Coefficient of Drag. The variation can be attributed to inconsistencies in computation or experimentation. This successfully validates the meshing techniques and computational methodology.

B. *Computational Results*

The velocity contours were plotted for all cases as depicted in Fig. 1. For a rear angle of 25°, it is evident that the flow closely adheres to the rear slant surface and from the vector plot in Fig. 1(a) and Fig. 1(d)., we can observe two strong counter-rotating vortices. The static pressure is seen to reach a value of approximately-90 Pa for an air velocity of 140km/h and around-210 Pa for a velocity of 180 km/h (Fig. 5).
The boundary separation reaches a maximum when the rear slant angle is 30° (Fig. 3(b) and Fig. 3(e)) and consequently decreases on further increase or decrease in slant angle, as observed. The increase in drag near 30° is due to the generation of two strong counter-rotating vortices which are formed by the separation of flow over the rear slanted surface. The static pressure is seen to suddenly change slightly after the onset of the rear slant surface (Fig. 6). There is a clear increase in the area of the wake region (Fig. 4(b) and Fig. 4(e)) as the vortices increase in size, as compared to lower and higher slant angles justifying a rear slant angle of 30° as the critical angle. The manifestation of two large, distinct eddies is also evident for this angle.
At higher angles, the flow behavior changes and C_d begins to decrease, due to the weakening of the counter-rotating vortices. For the rear slant angle of 35°, it is observed (Fig. 4(c) and Fig. 4(f)) that the counter-rotating vortices emanating in the C-pillar region have grown and fully developed further downstream within the wake region, but there is tendency for the larger vortices to break down into a number of smaller vortices. In Fig. 7, the static pressure at the trailing edge of the rear slant surface is seen to lie approximately between-270 Pa to-300 Pa, representing a larger pressure difference between the static pressures at the front and back of the Ahmed body, which accounts for the drag coefficient higher than the 25° case. Figure. 5 depicts the static pressure distribution around the Ahmed Body.

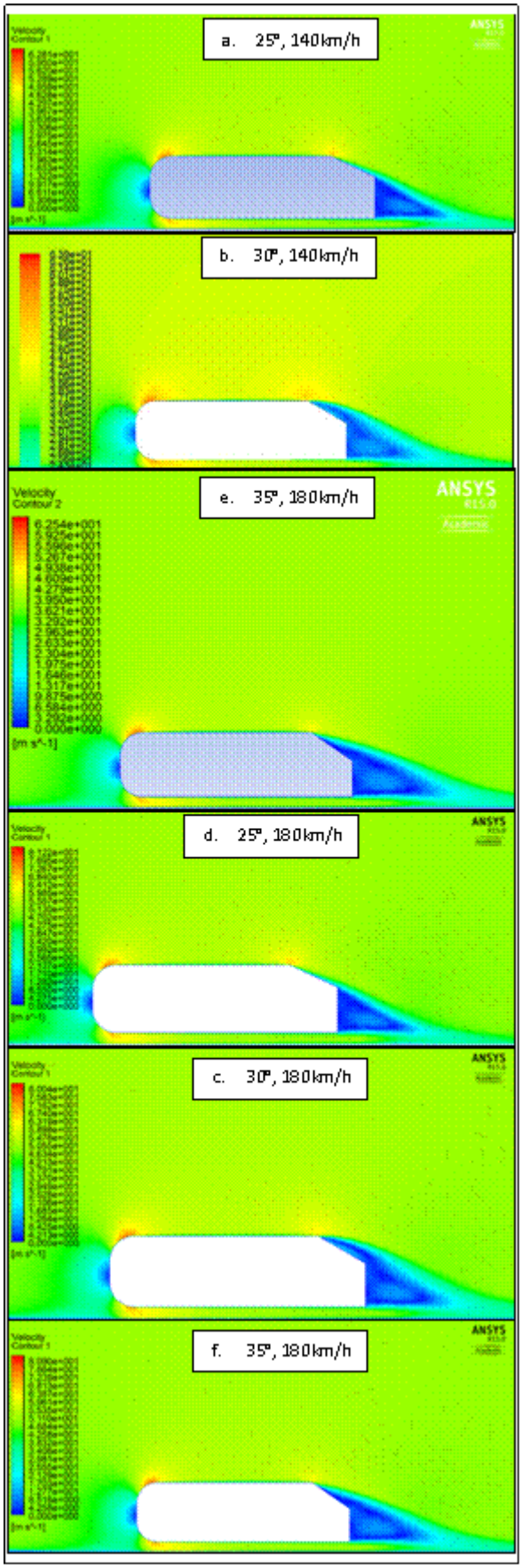

Fig. 3. Velocity Contours for all cases of the simulation

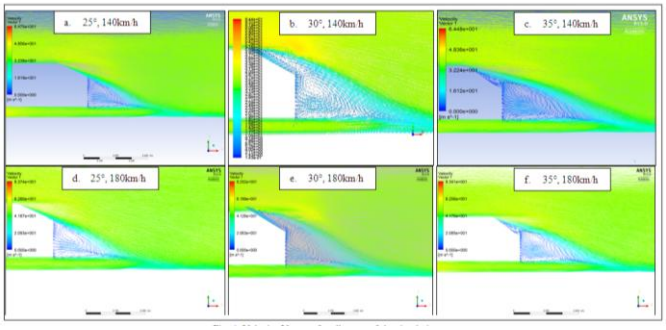

Fig. 4. Velocity Vectors for all cases of the simulation

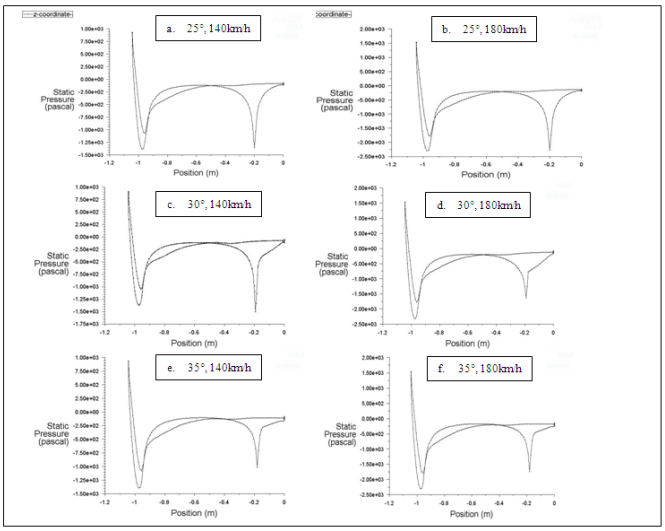

Fig. 5. Comparison of Static Pressure Distribution for all cases of the simulation

C. Acoustic Results

The sound pressure levels (SPL) were found for each case and are tabulated in Table 1 and Table 2. From the graphs depicted in Fig. 6-7, it was observed that the sound pressure levels follow a general trend of increasing with an increase in drag coefficient C_d. The SPL at the a-pillar for a velocity of 180 km/h and slant angle of 30° was found to be highest at 88 dB, whereas the highest SPL for the B-and C-pillars were 84 dB and 87 dB respectively, for the same rear slant angle and velocity. Noise levels were lowest for the lowest drag coefficient which was at 180km/h for the 25° case. In general, the noise levels at the a-pillar was found to slightly higher than those at the C-pillar, whereas those at the B-pillar were much lower owing to the absence of sudden change in geometry as is present at the A-and C-pillars.

Sound pressure levels were observed to be lowest for the bodies with a 25° rear slant angle, and highest for the 30° case. This is in concordance with the trends observed in drag coefficients, as found experimentally by Ahmed, which identify 30° as a critical rear slant angle. The drag coefficients were also found to follow the same trend thus providing a clear inference of an approximately direct correlation between drag coefficient and sound pressure levels.

Table 1: Sound pressure and drag coefficient results at 140km/h

Velocity	140 km/h								
Rear Slant Angle	25°			30°			35°		
Pillar	a	b	c	a	b	c	a	b	c
Drag Coefficient	0.30783	0.30783	0.30783	0.32313	0.32313	0.32313	0.31143	0.31143	0.31143
Sound Pressure Level (dB)	82	80	82.5	86.5	82.5	80	85	80.5	83

Table 2. Sound pressure and drag coefficient results at 180km/h

Velocity	180 km/h								
Rear Slant Angle	25°			30°			35°		
Pillar	a	b	c	a	b	c	a	b	c
Drag Coefficient	0.30369	0.30369	0.30369	0.32436	0.32436	0.32436	0.31655	0.31655	0.31655
Sound Pressure Level (dB)	82	80	82	88	84	87	85.5	81	84

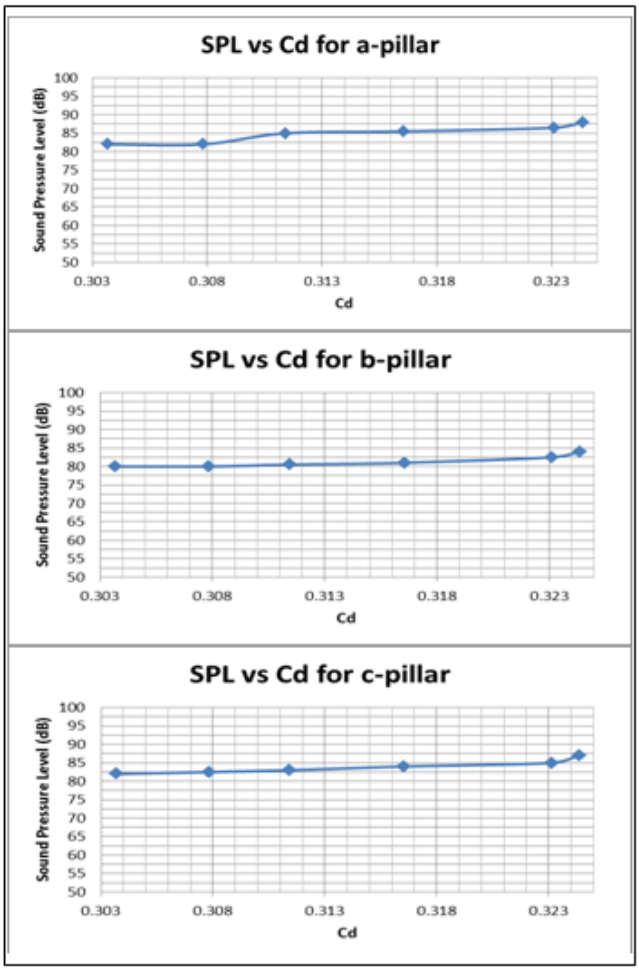

Fig. 6. Sound Pressure Level v/s drag coefficient at the 3 pillar regions

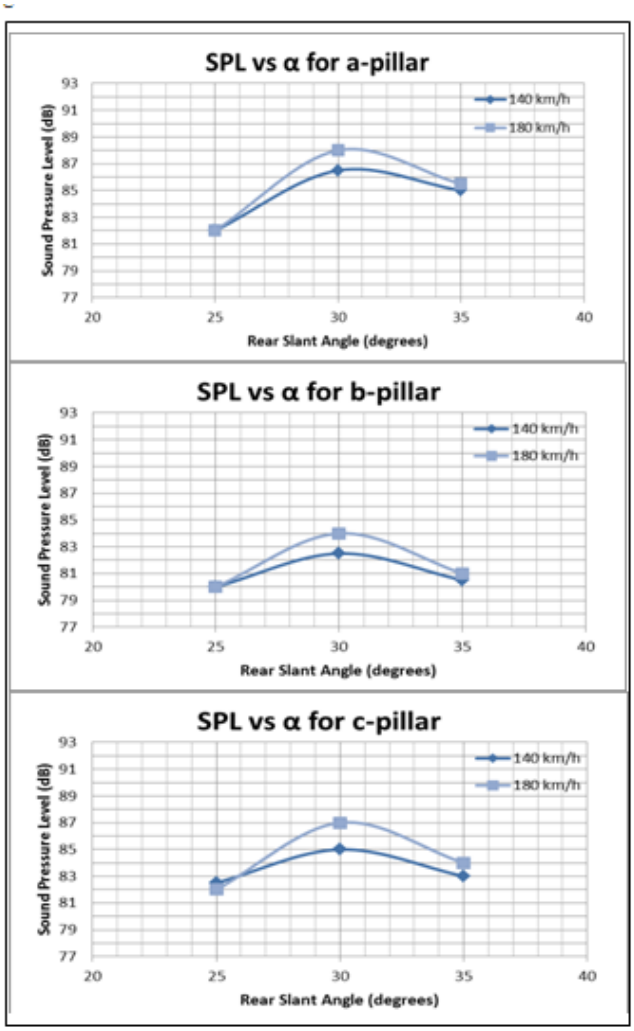

Fig. 7. Sound Pressure Level v's rear slant angle at 140km/h and 180km/h

IV. CONCLUSION

The relationship between drag and sound pressure levels were successfully investigated using computational methods. A general trend of increase in sound pressure levels with increasing drag was found. It was also understood that velocity was directly proportional to sound pressure levels in accordance with expectations. With the plotting of noise levels against rear slant angle, the relation between drag and sound pressure level was made more evident. Further improvements on the bluff body could include introducing a rough surface near the A and C Pillar regions to break the vortex shedding patterns, this could reduce both the drag as well as the acoustic signature.

ACKNOWLEDGMENT

We would like to thank VIT University for providing us with the laboratory facilities equipped with the authentic simulation resources, without which we would not have been able to undertake this research study.

REFERENCES

[1] S.R. Ahmed, G. Ramm, G. Faltin, Some salient features of the time-averaged ground vehicle wake, in: International Congress and Exposition, Detroit, Michigan, February 27-March 2, 1984, p. 840300.

[2] Bayraktar, D. Landman, O. Baysal, Experimental and computational investigation of Ahmed body for ground vehicle aerodynamics, in: International Truck and Bus Meeting and Exhibition Chicago, Illinois November 12-14, 2001, SAE Technical Paper Series, 2001-01-2742.

[3] H. Lienhart, C. Stoots, S. Becker, Flow and turbulence structures in the wake of a simplified car model (Ahmed model), in: Proceedings of the DGLR Fach. Symp. der AG STAB DGLR Fach. Symp. der AG STAB, Stuttgart University, 2000.

[4] B. Conan, J. Anthoine, P. Planquart, Experimental aerodynamic study of a cartype bluff body, Exp. Fluids 50 (2011) 1273-1284.

[5] Alam F, The effects of car a-pillar and windshield geometry and yaw angles on local flow and noise, PhD thesis, RMIT University, Melbourne; 2000.

[6] Mohsen AM, Experimental investigation of the wall pressure fluctuations in separated flows. Boeing Company Report D6-17094, USA; 1967.

[7] Watanabe M, Harita M, The effects of body shapes on wind noise. SAE paper no. 780266; 1978.

[8] Murad, Computational fluid dynamics of vehicle aerodynamics and associated acoustics. PhD thesis, Swinburne University, Melbourne; 2006.

[9] B. Lokhande, S. Sovani, J. Xu, Computational Aero-acoustic Analysis of a Generic Side View Mirror, SAE 2003-01-1698, 2003.

[10] Fluent 6.1 User's Guide, Fluent Inc., Lebanon, NH, 2003.

[11] J.E. Ffowcs Williams, D.L. Hawkins, Sound generation by turbulence and surfaces in arbitrary motion, Proceedings of the Royal Society of London A 264 (1969) 321-342.

[12] W. Layton A. Novotný, On Lighthill's acoustic analogy for low Mach number flows, New Dir. Math. Fluid Mech. (2010), 1-31

[13] G. Vino, S. Watkins, P. Mousley, J. Watmuff, S. Prasad, Flow structures in the near-wake of the Ahmed model, J. Fluids Struct. 20 (2005) 673-695.

[14] D.B. Sims-Williams, Self-excited aerodynamic unsteadiness associated with passenger cars, in: Ph.D. Thesis, University of Durham, 2001.

[15] Haruna S, Nouzawa T, Kamimoto I, Hiroshi S, An experimental analysis and estimation of aerodynamic noise using a production vehicle. SAE paper no. 900316, USA; 1990.

[16] Alam F, Zimmer G, Watkins S, Mean and time-varying flow measurements on the surface of a family of idealized road vehicles. Exp Therm Fluid Sci 2003; 27(5):639-54.

[17] George AR, Automobile aerodynamic noise, SAE paper no. 900315; 1990.

[18] Murad, Naser, Alam, Watkins, Computational fluid dynamics study of vehicle A-pillar aero-acoustics, Applied Acoustics 74 (2013) 882-896

[19] K. Ono, R. Himeno, T. Fukushima, Prediction of wind noise radiated from passenger cars and its evaluation based on auralization, Journal of Wind Engineering and Industrial Aerodynamics 81 (1999) 403-419.

[20] C. Tsai, L. Fu, C. Tai, J. Leong, Computational aero-acoustic analysis of a passenger car with a rear spoiler, Applied Mathematical Modelling 33 (2009) 3661-3673

[21] H. Dechipre, M. Hartmann, Aeroacoustics Simulation of an Automotive A-Pillar Rain Gutter, 4th European Automotive Simulation Conference (2009)

[22] David Roche and Ashok Khondge, Aero-Vibro Acoustics For Wind Noise Application, ANSYS Inc., Automotive Simulation World Congress Japan 2014